Quantum Computing in Green Energy Production

Mansour T.A. Sharabiani[1,*], **Vibe B. Jakobsen**[2], **Martin Jeppesen**[2], **and Alireza S. Mahani**[3]

[1]Imperial College of Science, Technology and Medicine, London, UK
[2]Nature Energy, Odense, Denmark
[3]Davidson Kempner Capital Management, New York, USA
[*]mansour.taghavi-azar-sharabiani05@imperial.ac.uk

ABSTRACT

Addressing the world's climate emergency is an uphill battle, requiring a multifaceted approach including optimal deployment of green-energy alternatives. Such undertakings often involve computationally-expensive optimisation of black-box models in a continuous parameter space. While recent hardware advances and the quantum advantage experiments have raised hopes for quantum computing (QC) to vastly outperform classical techniques on certain hard problems, real-world applications of QC have thus far been mostly confined to combinatorial optimisation problems such as graph partitioning, traffic routing and task scheduling, where parameter space is discrete and graph connectivity is sparse. Here we propose the quantum nonlinear programming (QNLP) framework for casting an NLP problem - in continuous space - as quadratic unconstrained binary optimisation (QUBO), which can be subsequently solved using special-purpose Ising-model solvers such as quantum annealers (QA) and coherent Ising machines (CIMs). QNLP consists of four steps: quadratic approximation of cost function, discretisation of parameter space, binary representation of discrete space, and solving the resulting QUBO. We derive and validate an upper bound on the error introduced by solving a discretised version of the cost function, based on the eigen-decomposition of the second-derivative (Hessian) matrix of the function. Linear and nonlinear constraints are incorporated into the resulting QUBO using slack variables and quadratic penalty terms. We proceed to apply our QNLP framework for optimisation of the daily feed rate of various biomass types at Nature Energy, the largest biogas producer in Europe. Biomass selection, if done optimally, increases the methane output of a biogas reactor, thus contributing to carbon-neutral energy production. Focusing on bound constraints only, the minimums of the high-dimensional, non-convex cost functions can be found theoretically, allowing for exact quantification of the quality of output produced by QNLP. For solving the QUBO, we use D-Wave's publicly-available quantum processing units (QPUs), accessible via Amazon Braket. We observe good performance on the DW-2000Q QPU - even using default settings - and higher sensitivity of performance to number of samples and annealing time for the Advantage QPU. These results are promising and potentially justify further investment in hardware, software, and optimisation research, in particular, in the area of solvers for dense QUBOs. QNLP can be used as a local-optimisation module in global algorithms such as the Trust Region family. Our proposed QNLP framework makes it possible to tackle continuous optimisation problems using emerging, special-purpose QUBO solvers. We thus hope that it provides a meaningful step towards overcoming the computational challenges posed by high-dimensional continuous-optimisation problems, especially those encountered in our battle against man-made climate change.

1 Introduction

In a declaration signed at the United Nations Climate Change Conference in 2019 (COP25), members of the World Biogas Association including Nature Energy - the largest producer of biogas in Europe - committed to delivering a 12% reduction in greenhouse gas (GHG) emissions by 2030[1]. The biogas industry - producing biomethane using anaerobic digestion (AD) of organic waste - has therefore become an important partner in the global campaign against climate change[2]. Biogas achieves this GHG reduction via multiple pathways such as replacing fossil fuels, avoiding methane slips from manure, storing carbon in soils, producing green fertilisers and enabling carbon re-use.

For a large biogas producer such as Nature Energy with a growing portfolio of plants and sourcing sites across Denmark and Europe, daily operations involve a plethora of complex decisions including sourcing, distribution, pre-tank storage and mixing of biomass in co-digestion tanks. Optimising such complex decisions can make a significant impact on the operational efficiency of the biogas plants and hence the long-term economic sustainability of the biogas industry. However, combinatorial explosion of the decision space in high-dimensional optimisation problems makes them computationally prohibitive, often exceeding the limits of classical computing platforms.

While drastic improvements in chip design and manufacturing, combined with increased parallelism of many-core CPUs, GPUs, FPGAs and cloud computing have delivered massive performance gains since the early days of computing, solving our most complex problems - such as optimising the operations of a network of biogas plants - requires further innovations by exploring alternatives to von-Neumann computing on semiconductors. This includes new computational frameworks using existing hardware, e.g., CMOS annealing[3,4], as well as entirely new approaches such as stochastic nanomagnets[5], coupled oscillatory networks[6], neuromorphic computing[7,8], optical parametric oscillators[9], and quantum computing (QC) using superconducting circuits[10,11], trapped ions[12], and photons[13].

In contrast to the von-Neumann architecture that is sequential and involves a clear separation of memory and computing, many of the special-purpose hardware platforms mentioned above can be described as distributed, in-memory computing that take advantage of the intrinsic parallelism of the underlying physical system. This often involves a tradeoff where speed is achieved at the expense of loss of generality. In particular, many designs such as CMOS annealers[14], coherent Ising machines[15] (CIMs) and quantum annealers[10] (QAs) specialise in finding the unconstrained minimum of the Ising-model energy function:

$$H(\sigma) = -\sum_{i,j} J_{i,j}\,\sigma_i\,\sigma_j - \sum_i h_i\,\sigma_i \tag{1}$$

where σ_i's are spin variables, taking values ± 1. Thus, to take advantage of such devices, we must express our optimisation problem in the Ising-model - or equivalently QUBO - form.

Consider the problem of selecting the daily rates for feeding various biomass types into a biogas plant, where the goal is to maximise the operating profits of the plant. This profit equals revenue from selling the renewable energy (biomethane) in the market, minus the cost of biomass. This is a high-dimensional, non-convex optimisation problem, where time needed to find the exact solutions would scale exponentially with problem size. Moreover, since daily feed rates are continuous variables, the optimisation problem - in its original form - is not a QUBO. We use the phrase 'nonlinear programming' (NLP) to refer to optimisation problems with a continuous parameter space.

In this paper, we develop a general mathematical framework for converting NLP problems - e.g., the biomass selection problem - to QUBOs, thus allowing the use of special-purpose devices such as QA. We refer to our framework as quantum nonlinear programming or QNLP. It consists of 4 steps: 1) quadratic approximation of the NLP cost function, 2) discretisation of parameter space, 3) binary representation of each discrete variable, and 4) solving the resulting QUBO using QA, CIM or other Ising-model solvers.

An important property of QNLP is that, for a cost function with a fully-dense Hessian (second derivative) matrix, the resulting QUBO's interaction matrix will also be fully-dense (Result 2). Benchmarking studies[9] using MAXCUT and Sherrington-Kirkpatrick spin-glass[16] models found that fully-dense matrices pose challenges for CIM and particularly QA, which is expected due to limited connectivity of the quantum bits (or qubits) in a D-Wave QA. Our experiments with the biomass selection problem on D-Wave QPUs confirm these previous findings, but also point to interesting distinctions between the different QPU architectures.

We are hopeful that this work helps create a platform for further research on using special-purpose devices such as quantum annealers for solving important optimisation problems that we face in our fight against the climate emergency.

2 Results

2.1 Nature Energy's Biomass-Selection Optimisation Problem

In a Continuously-Stirred Tank Reactor (CSTR) at an industrial-scale biogas plant, several types of biodegradable material - or biomass - are continuously fed into the reactor where, with the help of bacterial micro-organisms, they undergo a complex, multi-stage process known as anaerobic digestion (AD)[17], at the end of which green energy is produced in the form of biomethane. Biomasses have diverse attributes in terms of the amount and rate of methane production, procurement and transportation costs, and regulatory implications such as qualification of digestate for organic farming, and eligibility for subsidies. Figure 1 illustrates some of this diversity, using data collected by Nature Energy, the largest producer of biogas in Europe. (For details on Nature Energy data, see Section 4.1).

In this paper, we focus on the biomass selection problem in a biogas reactor, where the goal is to set the daily rate for feeding each biomass into the reactor. We further assume that each type of biomass produces biomethane in the CSTR according to the production curves fitted to data collected during biomethane potential (BMP) lab experiments (see Section 4.1). The single time parameter used - across all biomass types - to read out the BMP data is the Hydraulic Retention Time (HRT) of the reactor, which is defined as the ratio of the active reactor volume over the total daily volume of biomass flowing through the reactor,

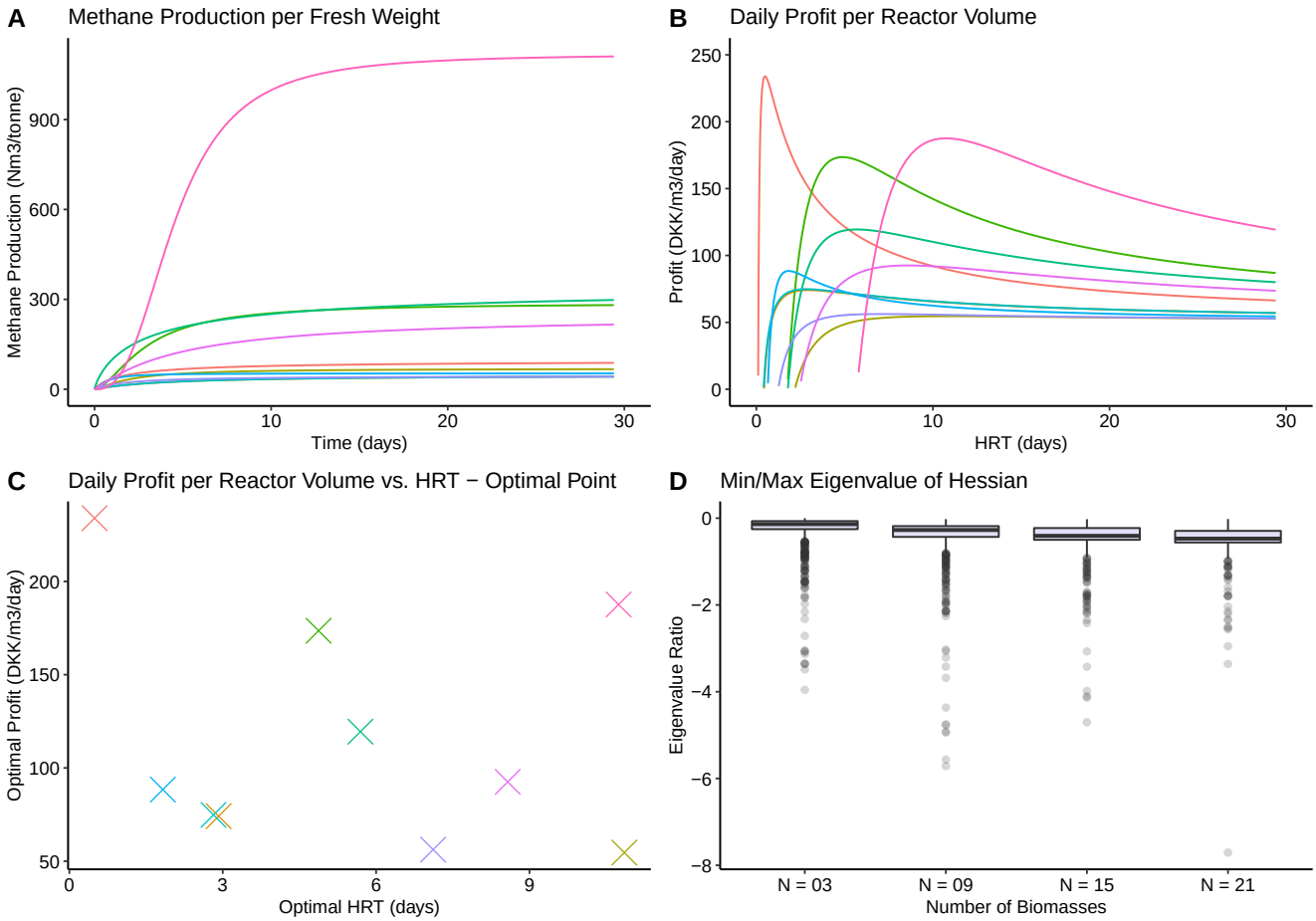

Figure 1. Biomass Selection Problem for Nature Energy. **A**: Bio-methane potential curves (per fresh weight) for 10 of the 28 biomasses used in experiments of Section 2.3. **B**: Profitability (per reactor volume per day) vs. Hydraulic Retention Time (HRT) for the same group of biomasses. **C**: Scatter plot of maximum daily profit per reactor volume vs. optimal HRT. **D**: Ratio of smallest to largest eigenvalue of the Hessian (second derivative) matrix for the cost function. Each bar is based on 1000 random samples of biomasses (N of 28). For each sample, the first element of $\mathbf{x}_0$ is chosen to be the univariate optimal value for the first biomass (see Section 4.2.2), and the remaining elements are set to zero. Biomass properties are collected and provided by Nature Energy. Note that the profit numbers (y-axis) in panels **B** and **C** have been adjusted with a constant offset to protect business sensitive information.

Biomass	G0	k	n	cost
Corn	115	0.74	1.23	270
Manure - cow	16	0.4	1.13	75
Manure - pig	15	0.43	1.12	72
Manure - sow	10	0.43	1.12	69
Organic manure - cow	16	0.4	1.13	75
Organic manure - pig	15	0.43	1.12	72
...	...	...	...	...
...	...	...	...	...

Table 1. Representative biomass data from NE. G0, k, n are the parameters of the cone model (Section 4.2.1) for biomethane production. Units: G0 - Natural m^3 of methane per tonne of fresh biomass; k: day^{-1}; n: dimensionless; 'cost' - DKK per tonne of fresh biomass. To avoid unintended business competitive impact, 1) only data for 4 of 28 biomass types used in the paper are displayed here as examples, and 2) cost figures have been slightly modified.

and can be interpreted as the average time each biomass spends in the CSTR. The above assumptions lead to the following expression for the cost function, which is the total daily cost of sourcing the biomass, minus the daily revenue from selling the biomethane produced in the reactor:

$$f(\mathbf{x}) = \mathbf{x}^\top (\mathbf{c} - r\mathbf{Y}(X)), \quad x_k \geq 0, \quad \forall k = 1,\ldots,K. \tag{2}$$

where $\mathbf{x}$ is a vector of length K representing daily flow volume of each biomass into the reactor, X is the total daily feed, i.e., $X \equiv \sum_k x_k$, and $\mathbf{Y} \equiv \begin{bmatrix} Y_1(X) & Y_2(X) & \cdots & Y_K(X) \end{bmatrix}$, with Y_k's representing parametric yield functions. (Note that $HRT = V/X$, where V is the total active volume of the reactor, and hence yield functions could also be expressed in terms of reactor HRT.) In this paper, we use the cone model[18] for fitting the BMP experiments (section 4.2). Financial parameters $\mathbf{c}$ and r represent the (constant) unit cost of each biomass and the revenue per unit of methane produced, respectively. Throughout the paper, we use $r = 6.0 DKK/m^3$. As a reasonable approximation, we assume a mass density of 1.0 (fresh tonnes per m3) - i.e., same as water - for all biomass types entering the reactor. This allows us to use weights and volumes interchangeably.

The above cost function has two important properties. First, it is non-convex, which means there are many places in the parameter space where the Hessian (of the cost function) has negative eigenvalues. Panel **D** of Figure 1 illustrates this point. Optimisation of non-convex cost functions, even in the quadratic form, is an non-deterministic polynomial-time (NP)-hard problem[19]. Second, the minimums of the cost function of Eq. 2 can be identified mathematically, per below.

Result 1. *For cost function of form 2, all minimums - global and local - are single-ingredient, i.e., they must satisfy* $\sum_k \mathrm{I}[x_k > 0] \leq 1$. *I() is the indicator function.*

Proof. We use proof by contradiction. Consider a multi-ingredient point $\mathbf{x}$, i.e., $\sum_k \mathrm{I}[x_k > 0] = m > 1$. Assume that k_1 is the ingredient with the largest value of $rY_k(X) - c_k$ among the set of non-zero ingredients, $U = \{k_1, k_2, \ldots, k_m\}$. Consider a small step d$\mathbf{x}$ such that $dx_k = 0, k \notin U$ & $dx_k < 0, k \in U, k \neq k_1$ & $dx_{k_1} = -\sum_{k' \in U, k' \neq k_1} dx_{k'} > 0$. Such a step keeps X constant, i.e., $dX = \sum_k dx_k = 0$. Furthermore, since the expression inside the parentheses in Eq. 2 remains constant, the change in f is given by $df = \sum_k (c_k - rY_k(X))\, dx_k$, which can be re-arranged to have $df = \sum_{k' \in U, k' \neq k_1} \left\{ (c_{k'} - rY_{k'}(X)) - (c_{k_1} - rY_{k_1}(X)) \right\} dx_{k'}$. The very definition of k_1 means all expressions in parentheses are non-negative, and since all dx_k's are negative, we must have $df \leq 0$. Therefore, $\mathbf{x}$ cannot be a local minimum of f. As such, f will have - at most - K local, single-ingredient minimums, one or more of which will be the global minimum. □

To put it in less mathematical terms, any multi-ingredient solution can be improved upon by replacing all sub-optimal ingredients with the optimal one while keeping the HRT - or equivalently X - constant. Since the optimal ingredient is only a function of HRT, we can continue this substitution until we have made a full switch to the optimal biomass. The crucial requirement is that the ranking of biomasses does not change as we change $\mathbf{x}$ while keeping X constant. A sufficient condition for this to happen is to have constant marginal cost ($\mathbf{c}$) for all biomasses, e.g., no volume discounts or supply limits.

In summary, thanks to Result 1, the problem of minimising the K-dimensional cost function in Eq. 2 is reduced to minimising K, one-dimensional cost functions, which is computationally feasible. As such, the utility of Result 1 is that, by effectively providing the theoretical location of function minimums, it allows for accurate benchmarking of our proposed QNLP algorithm.

2.2 Quantum Nonlinear Programming (QNLP)

The first step in QNLP is the quadratic approximation of the twice-differentiable cost function using a second-order Taylor-series expansion in the neighborhood of a starting point, as is done in sequential quadratic programming[20] (SQP) and trust region (TR) methods[21]. Second, the continuous parameter space is approximated with a discrete grid covering a rectangular neighborhood, centered on the starting point. Third, a binary basis is used to represent the discrete steps in each dimension. The result is a quadratic binary optimisation problem. Bound constraints can be incorporated via a suitable choice of grid boundaries, while any additional, linear constraints can be handled using slack variables. Nonlinear constraints are first converted to linear ones using first-order Taylor-series expansion of the constraint function.

The combined effect of the above three steps - quadratic approximation, discretisation and binarisation - is to transform the original NLP problem into a QUBO, which can be subsequently given to a special-purpose QUBO solver such as CIM or QA. An overview of the QNLP framework is illustrated in Fig. 2. Note that QNLP is, by nature, a local optimisation algorithm which can be embedded in global algorithms such as TR. We develop the equations for the base case - i.e., only bound constraints - below. Extension to general constraints - linear and nonlinear - can be found in Section 4.3.

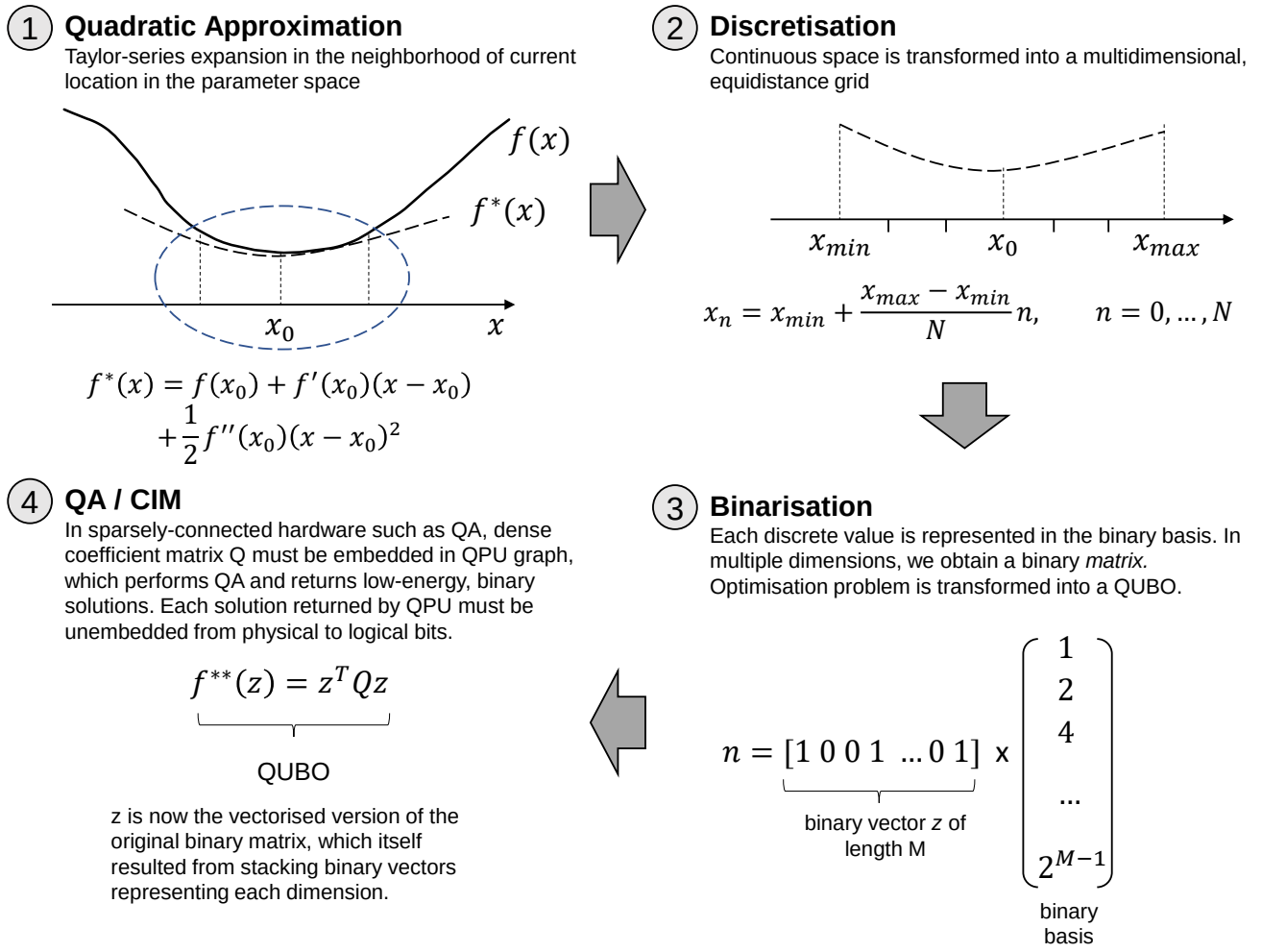

Figure 2. Outline of the QNLP framework - illustrated using the one-dimensional case - for converting a NLP problem to a QUBO, to be solved via special-purpose QUBO solvers such as CIM and QA. See Section 2.2 for details.

Consider the following NLP problem

$$\begin{aligned} \min_{\mathbf{x}} \quad & f(\mathbf{x}) \\ \text{s.t.} \quad & a_k \leq x_k \leq c_k \quad \forall k \in \{1, \ldots, K\} \end{aligned} \tag{3}$$

where f is defined on $F \subseteq \mathbb{R}^K$. In the neighborhood of $\mathbf{x}_0 \in F$, we have the following quadratic approximation for $f(.)$:

$$f^*(\mathbf{x}) = f_0 + \mathbf{g}_0^\top (\mathbf{x} - \mathbf{x}_0) + \frac{1}{2} (\mathbf{x} - \mathbf{x}_0)^\top \mathbf{H}_0 (\mathbf{x} - \mathbf{x}_0) \tag{4}$$

where f_0, $\mathbf{g}_0$ and $\mathbf{H}_0$ are the cost function, its gradient vector (first derivative) and its Hessian matrix (second derivative), respectively, all evaluated at $\mathbf{x} = \mathbf{x}_0$. Discretisation can be achieved using the following transformation:

$$\mathbf{x}(\mathbf{n}) = \mathbf{a} + \Delta \mathbf{n} \tag{5}$$

where $\mathbf{a}$ is the vector of lower bounds for $\mathbf{x}$, Δ is a diagonal matrix of size K constructed from the range vector $\delta = (\mathbf{c} - \mathbf{a})/N$, i.e., $\Delta = \text{diag}(\delta)$. ('diag' is an operator that creates a diagonal matrix from a vector.) $\mathbf{n}$ is an integer vector of length K, with each element in the range $[0, N]$, i.e., $\mathbf{n} \in \{0, 1, \ldots, N\}^K$. Finally, we use a binary representation for each element n_k in $\mathbf{n}$:

$$n_k = \mathbf{b}^\top \mathbf{z}_k \tag{6}$$

where $\mathbf{b}$ is the M-digit binary basis $\begin{bmatrix}1 & 2 & \cdots & 2^{M-1}\end{bmatrix}^\top$, and $\mathbf{z}_k$ is a binary vector of length M, representing the range of integers $[0, 2^M - 1]$. (As such, we require $N+1$ to be a power of two.) To represent the vector $\mathbf{n}$, we stack $\mathbf{z}_k$'s row-wise to form a $K \times M$ matrix $\mathbf{Z}$:

$$\mathbf{n} = \mathbf{Z}\,\mathbf{b}. \tag{7}$$

Combining Eqs. 5 and 7, and using the vectorisation or *vec* trick (see Section 4.3.1), we obtain:

$$\begin{cases} \mathbf{x} - \mathbf{x}_0 & = \mathbf{d} + \mathbf{A}\,\mathbf{z} & \text{(8a)} \\ \mathbf{d} & = \mathbf{a} - \mathbf{x}_0 & \text{(8b)} \\ \mathbf{A} & = \mathbf{b}^\top \otimes \Delta & \text{(8c)} \end{cases}$$

where $\mathbf{z}$ is a binary vector of length KM, resulting from stacking columns of $\mathbf{Z}$, and $\otimes$ is the Kronecker product. Using the above substitution in Eq. 4 leads to the following QUBO:

$$\min_{\mathbf{z}} \quad \mathbf{z}^\top \mathbf{Q}\,\mathbf{z} \tag{9}$$

with:

$$\mathbf{Q} = \frac{1}{2}\mathbf{A}^\top \mathbf{H}_0\,\mathbf{A} + \operatorname{diag}\left(\mathbf{A}^\top(\mathbf{g}_0 + \mathbf{H}_0\,\mathbf{d})\right) \tag{10}$$

Further details on the above derivation, as well as generalisation for linear and nonlinear inequality and equality constraints, are given in the Section 4.

As mentioned in Section 1, denseness of $\mathbf{Q}$ is important, which motivates the following result. Proof is provided in Section 4.3.2.

Result 2. *For a fully-dense but otherwise arbitrary Hessian matrix* $\mathbf{H}_0$*, the coefficient matrix* $\mathbf{Q}$ *given by Eq. 10 is also fully-dense.*

The computational cost of $\mathbf{Q}$ in Eq. 10 is dominated by the term $\mathbf{A}^\top \mathbf{H}_0\,\mathbf{A}$. Using Eq. 27 (Section 4.3.2), and noting that each element of $\Delta\mathbf{H}_0\Delta$ can be calculated in $O(1)$ thanks to Δ being diagonal, the cost of calculating $(\mathbf{b}\,\mathbf{b}^\top) \otimes (\Delta\mathbf{H}_0\Delta)$ is $O(K^2M^2)$, which is polynomial in problem size, K. Furthermore, if we take advantage of $b_m = 2^{M-1}$, this can be reduced to $O(K^2M)$, since number of unique elements of $\mathbf{b}\,\mathbf{b}^\top$ is reduced from $O(M^2)$ to $O(M)$.

While the third step, i.e., binary representation of the discrete grid is an exact or error-free step, same cannot be said of the first two steps: quadratic approximation, and discretisation.

2.2.1 Quadratic Approximation

Selecting neighborhood size (Δ) for quadratic approximation (Eq. 4; Figure 3, panel **A**) involves a tradeoff: small values lead to small steps and hence slow convergence, while large steps run the risk of large deviations between quadratic approximation and exact function values, which in turn can lead to inefficient, or even counter-productive, steps (Figure 3, panel **B**). TR algorithms manage this tradeoff via dynamic expansion and contraction of neighborhood size based on closeness of approximate and exact function values in the prior step[22]. In this paper, we focus on QNLP as a local-optimisation module that can be incorporated into global algorithms such as TR; therefore, topics such as dynamic neighborhood adjustment, and more generally embedding QNLP into global algorithms are deferred to future research. See Section 3 for a discussion.

2.2.2 Discretisation

Intuitively, optimising a discretised version of a 'smooth' function should produce results that are similar to optimising the exact function, where smoothness can be defined using Lipschitz continuity[23]. In particular, if the first or second derivative of a function are absolute-bounded, true function minimum - potentially lying in-between the discrete-grid nodes - cannot be much lower than the observed minimum.

To illustrate the point, consider the one-dimensional case of Figure 3 (panel **C**). The worst-case scenario is for two adjacent nodes on the grid to both be the apparent minimums of a discretised, convex function, and for the absolute minimum - on the continuous scale - to lie halfway between the nodes. It is easy to see that the discretisation error, in this case, is $\frac{1}{8}\lambda\delta^2$, where λ is the (positive) second derivative of the quadratic cost function and δ is grid resolution. The result below generalises this result to the multivariate case. Proof is given in Section 4.3.

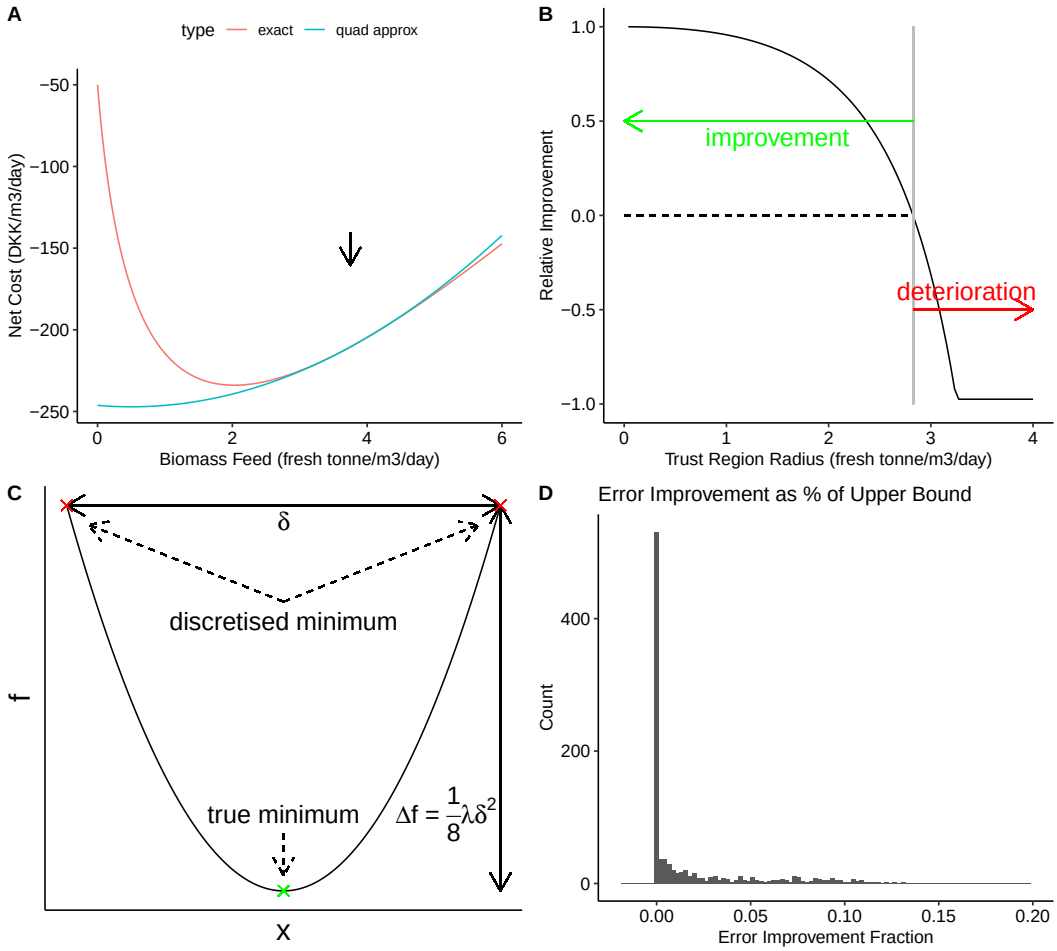

Figure 3. **A**: Exact vs. quadratic-approximation cost function for an example biomass. Vertical arrow shows the reference point ($\mathbf{x}_0$) used for the quadratic approximation (blue line) of the cost function (red line). **B**: Relative improvement as a function of neighborhood radius, centered on same value indicated in panel **A**. Consistent with TR literature, relative improvement is defined as the ratio of actual to expected (based on quadratic approximation) reduction in cost function. When trust region is expanded beyond the grey vertical bar, the optimisation step based on the quadratic approximation increases the cost function, rather than decrease it. **C**: Illustration of the upper bound on discretisation error - defined in Result 3 - in the univariate case. λ is the largest positive eigenvalue of the Hessian, which is also the second derivative of the function resulting from the intersection of the quadratic fit with a vertical plane. See text for details. **D**: Observed error improvement as a fraction of upper bound, confirming that the upper bound is never violated (fraction is always smaller than one.) Note that the y-axis values in panel **A** have been adjusted with an offset to protect sensitive business information.

Result 3. *Discretisation error resulting from solving the QUBO in Equation 10 rather than the underlying quadratic function of Eq. 4 in continuous space, has an upper bound of* $\frac{1}{8}\lambda\,\delta^\top\delta$*, where* λ *is the maximum of largest positive eigenvalue of* $\mathbf{H}_0$ *(if there is one) and zero, and* δ *is the grid resolution vector.*

The above result can be used in selecting grid resolution (δ) in each step, using a 'natural' scale or resolution (Δf) for the cost function: $\delta = (8\Delta f/\lambda)^{1/2}$ (assuming an isotropic grid).

2.3 QNLP using QA

The last step in QNLP is solving the QUBO that results from the sequence of quadratic approximation, discretisation, and binarisation (Eq. 10). Ongoing research on special-purpose devices such as CMOS annealers, CIMs and QAs promises to yield high-performance, QUBO solvers in the next few years, with improved bit count, connection density and fidelity. For the time being, we illustrate the application of QNLP to our biomass selection problem using D-Wave's publicly-available QPUs.

2.3.1 Setup

D-Wave offers two QPUs for public access[24]: 1) the *DW-2000Q* system (version 6) with 2,048 qubits connected in the 'chimera' pattern, and 2) the *Advantage* system (version 1.1) with 5,760 qubits, connected in the 'pegasus' pattern. *Advantage* has both higher qubit count and more connections per qubit than *DW-2000Q*, thus allowing for embedding of larger and denser matrices with shorter chain lengths.

The QPUs can be accessed via D-Wave's cloud service called Leap[25], and also through Amazon Braket on AWS. The advantage of the second option is a unified API for accessing multiple quantum computing hardware providers such as D-Wave, IonQ and Riggeti, as well as the AWS quantum simulators. We used Amazon Braket for experiments reported in this paper.

Ideally, solving a QUBO would be as simple as submitting the coefficient matrix - $\mathbf{Q}$ - to the QPU, and getting back the exact minimum of the quadratic cost function, $\frac{1}{2}\mathbf{z}^\top \mathbf{Q}\mathbf{z}$. In reality, however, QA is an imperfect, multi-step process that includes 1) embedding $\mathbf{Q}$ in the QPU working graph, 2) quantum annealing, and 3) unembedding the results. Each step involves several control parameters, and obtaining the best results requires a minimal understanding of the implementation. For a brief overview of QA on D-Wave and its key control parameters, see Section 4.4.

2.3.2 Embedding and Problem Size

For a fully-connected device such as CIM, there would be no distinction between logical and physical bits. However, due to the limited connectivity of a D-Wave QPU and hence the need for embedding, multiple qubits are needed to represent each logical bit in a dense problem. As Fig. 4 shows, the number of qubits used for each bit grows linearly, with the slope of the line for the DW-2000Q QPU being nearly twice that of the Advantage QPU. In particular, while the largest, fully-dense matrix that can be embedded in DW-2000Q is 63 bits, the Advantage QPU can handle fully-dense matrices more than twice that size. (The exact numbers would depend on the embedding algorithm, the yield of the QPU working graph, and random initialisation of the embedding algorithm.)

Comparing *clique* and *minorminer* libraries for embedding (Figure 4) shows that the *clique* library creates slightly shorter chains (left panel) with more homogeneous lengths (right panel). In particular, clique embedding on *DW-2000Q* creates chains of nearly identical lengths.

As discussed in Section 4.3.6, introduction of slack variables for handling inequality constraints causes the coefficient matrix to become sparse, which would allow larger interaction matrices to be embedded in the QPUs, compared to the fully-dense matrices resulting from problems with bound constraints only.

2.3.3 Performance testing using Default Settings

Tuning all the control parameters of D-Wave QPUs (Section 4.4.2) is infeasible in most practical settings. Other than the default settings of D-Wave libraries, we made three explicit decisions: 1) *minorminer* for embedding library, 2) 1000 annealing samples or reads, and 3) using the 'scaled' method of setting chain strength, with multiplier values following the geometric series {5e-5, 5e-4, 5e-3, 5e-2, 5e-1, 1}.

Figure 5 shows the results. *DW-2000Q* achieves near-perfect performance for a broad range of chain strength parameters, and across all problem sizes tested (up to the maximum possible value of 63 bits). The *Advantage* performance starts to drop significantly at 45 bits (15 biomasses and 3 bits per biomass). For both devices, best performance is achieved with chain break probabilities as high as $\sim$80%, with the average number being 53% and 32% for *DW-2000Q* and *Advantage* QPUs, respectively.

The relatively lower performance of the newer *Advantage* device - despite its higher qubit count and connectivity - raises the question of whether adjusting the control parameters of this device would help close the performance gap with the *DW-2000Q* device. Below we study the performance sensitivity of *Advantage* to various parameters for 10 randomly-generated problems with 21 biomasses (and $M = 3$), which is the maximum size achievable on *DW-2000Q*.

2.3.4 Sensitivity Analysis for Advantage QPU

We studied the effect of six important parameters that control the QA process on a D-Wave QPU. The parameters and their values tested in our experiments are listed in Table 2 and described in Section 4.4.2. We conducted six experiments, varying one of the above control parameters in each one while holding the others fixed.

Figure 6 shows the results. There are a few key takeaways from our experiments:

1. For 3 out of 10 runs where the performance under default settings is perfect, we see virtually no sensitivity to the values of control parameters. This is indicated by the horizontal green line at $y = 0$ in Figure 6.

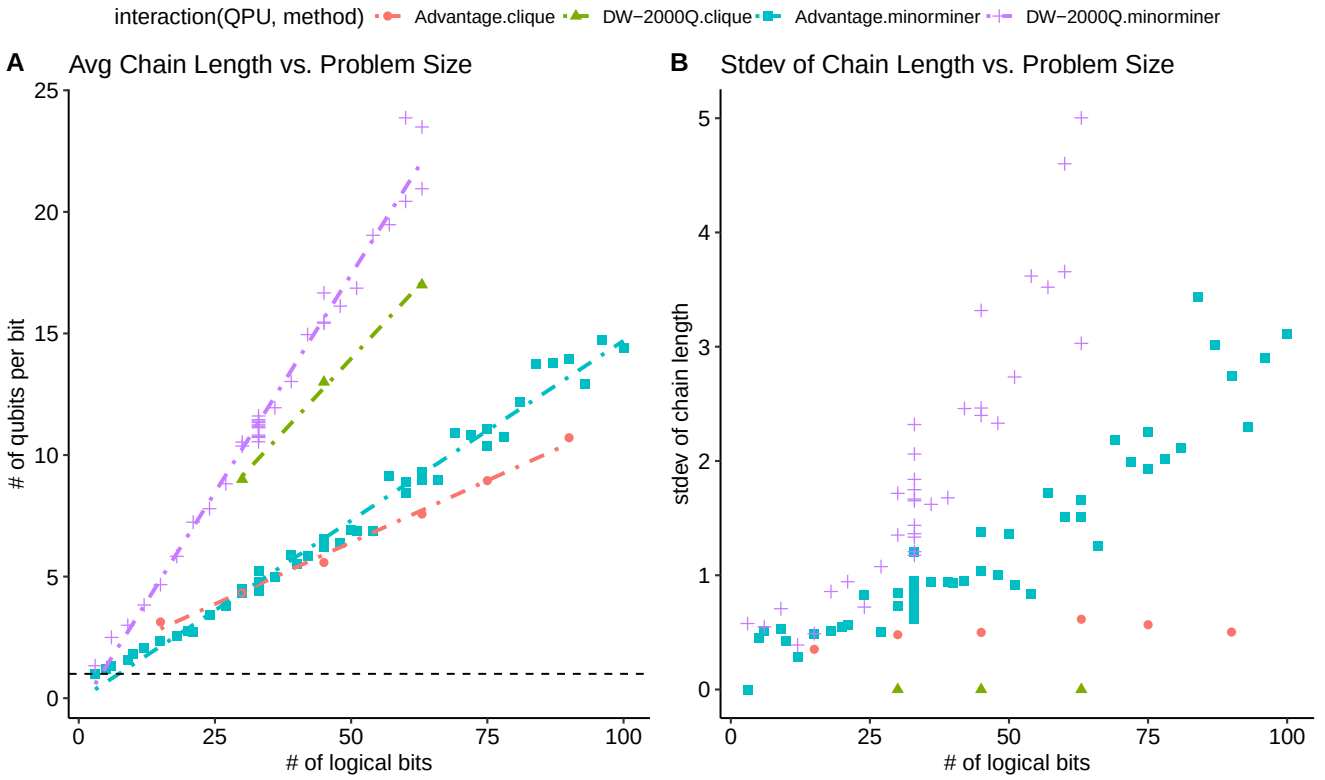

Figure 4. Minor embedding of fully-connected graphs of varying sizes in the working graphs of D-Wave's QPUs. **A**: Average chain length (or number of qubits per bit) vs. problem size. Dashed horizontal line indicates the ideal outcome - using a fully-connected QPU - where only one qubit is used per bit, regardless of problem size. **B**: Standard deviation of chain length (within a single embedded graph) vs problem size. *Minorminer* and *clique* embedding were applied to *Advantage* and *DW-2000Q* devices.

2. Of the six control parameters tested, only two exhibit a clear impact on performance: Number of samples, and annealing time. Increasing either one improves performance, a result which agrees with our expectations. However, in neither case we find the best results to match those of the *DW-2000Q* QPU.

3. W did not see a significant impact from the choice of embedding library (*minorminer* vs. *clique*), post-programming and readout thermalisation times, or the number of spin-reversal transforms. Consistent with these results, we also did not see a significant drop in sample quality.

Parameter	Range/Values	1	2	3	4	5	6
Embedding library	M, C	**M,C**	M	<-	<-	<-	<-
Number of reads	1-1e4	1e3	**1e2,1e3,1e4**	1e2	1e3	1e2	<-
Annealing time (μsec)	1-2e3	2e1	<-	**2e1, 2e2, 2e3**	20	<-	<-
Programming thermalisation (μsec)	0-1e4	1e3	<-	<-	**1e1,1e2,1e3,1e4**	1e3	<-
Readout thermalisation (μsec)	0-10,000	0	<-	<-	<-	**0,50,250,1250,6250**	0
Spin reversal transforms	0 - <number of reads>	0	<-	<-	<-	<-	**0,1,5,25,100**

Table 2. List of key control parameters for D-Wave QPUs. For definition of these and other parameters, see Section 4.4. Columns 1-6 indicate the values of each parameter used for each experiment. Values in bold correspond to the parameter whose value was varied in that experiment. The symbol '<-' means same value as prior experiment was used. Abbreviations: D = discard, MV = majority vote, WR = weighted random, ME = minimise energy, S = Scaled, UTC = Uniform Torque Compensation, M = minorminer, C = clique

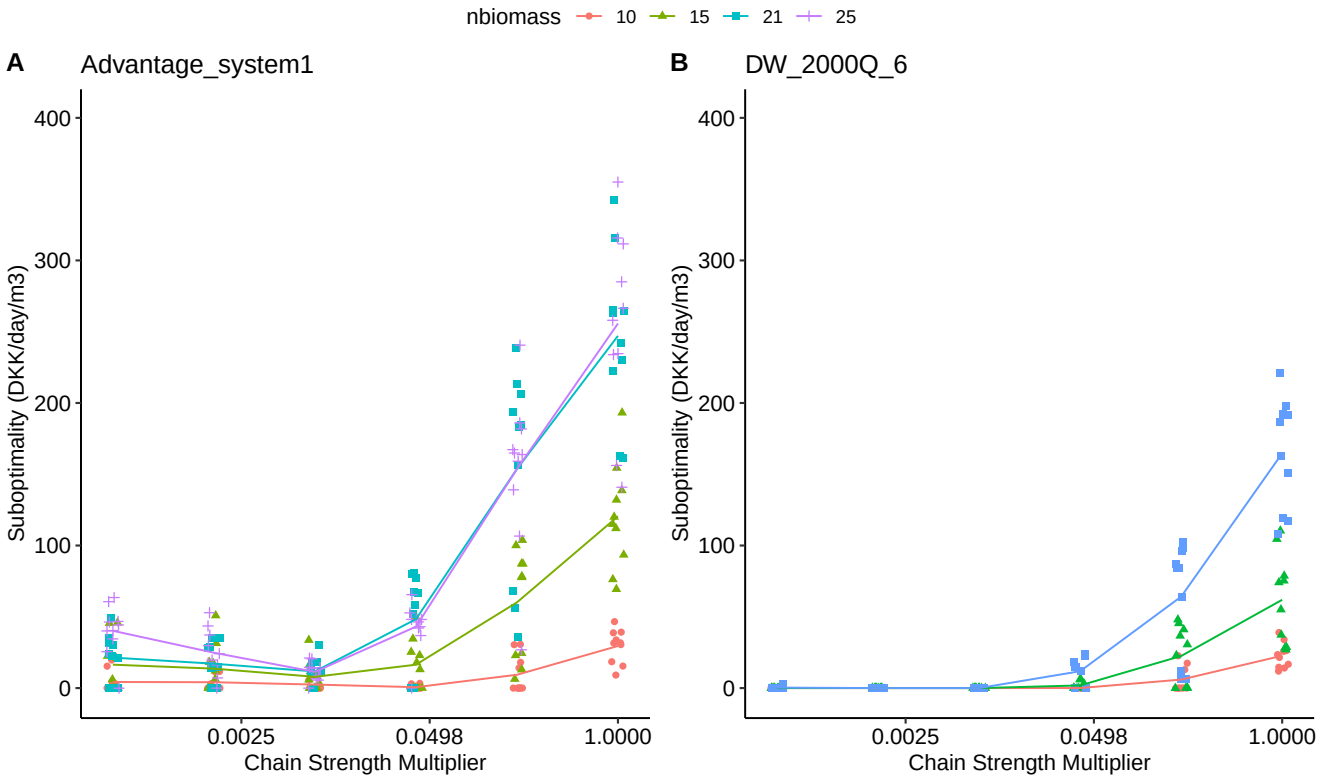

Figure 5. Performance of *Advantage* (left) and *DW-2000Q* (right) QPUs for a range of problem sizes and chain strength multipliers. We used the 'scaled' function to calculate the baseline chain strength parameter. For a given problem size, ten problems were used across all values of chain strength multiplier. We used $M = 3$ bits per dimension for discretisation; therefore, problem sizes tested are 30, 45, 63, and 75 bits, with the last value tested for *Advantage* only.

2.3.5 A Note on Timing

In the above results, we did not discuss the timing of running QA tasks. Using a shared resource such as D-Wave's public QPUs adds significant overhead to runtimes. For example, a typical QA task could take more than 20 seconds end-to-end, with only 1 second of it being spent on the core QA task itself. In iterative/global algorithms, such overhead would render the algorithm impractical. Embedding can be another time-consuming step. Fortunately, for fully-dense matrices, embedding can be pre-calculated once for each problem size. We expect that with broader accessiblity of D-Wave QPUs and other hardware, such overhead is reduced and genuine speedups for quantum algorithms compared to their classical counterparts can be tested and verified.

3 Discussion

We introduced the QNLP framework for optimisation of a continuous cost function by converting it to a QUBO, and using a special-purpose, Ising solver - such as quantum annealers or coherent Ising machines - to optimise the resulting problem. The NLP-to-QUBO conversion involves three steps: 1) quadratic approximation of cost function, 2) discretisation of the continuous parameter space, and 3) binary representation of each discretised parameter (Figure 2). We applied the QNLP framework to the biomass selection problem for the largest biogas producer in Europe - Nature Energy, using D-Wave's publicly-available quantum processing units.

In some applications, a single iteration of QNLP could be sufficient, e.g., when any adjustments to current operating conditions of an industrial or business process must be small and incremental. This could be, for instance, due to uncertainties in extrapolating the various black-box models that feed into the cost function beyond their historical range of parameters. In other words, the permissible search radius around the current point in the parameter space may be small enough to justify a quadratic approximation.

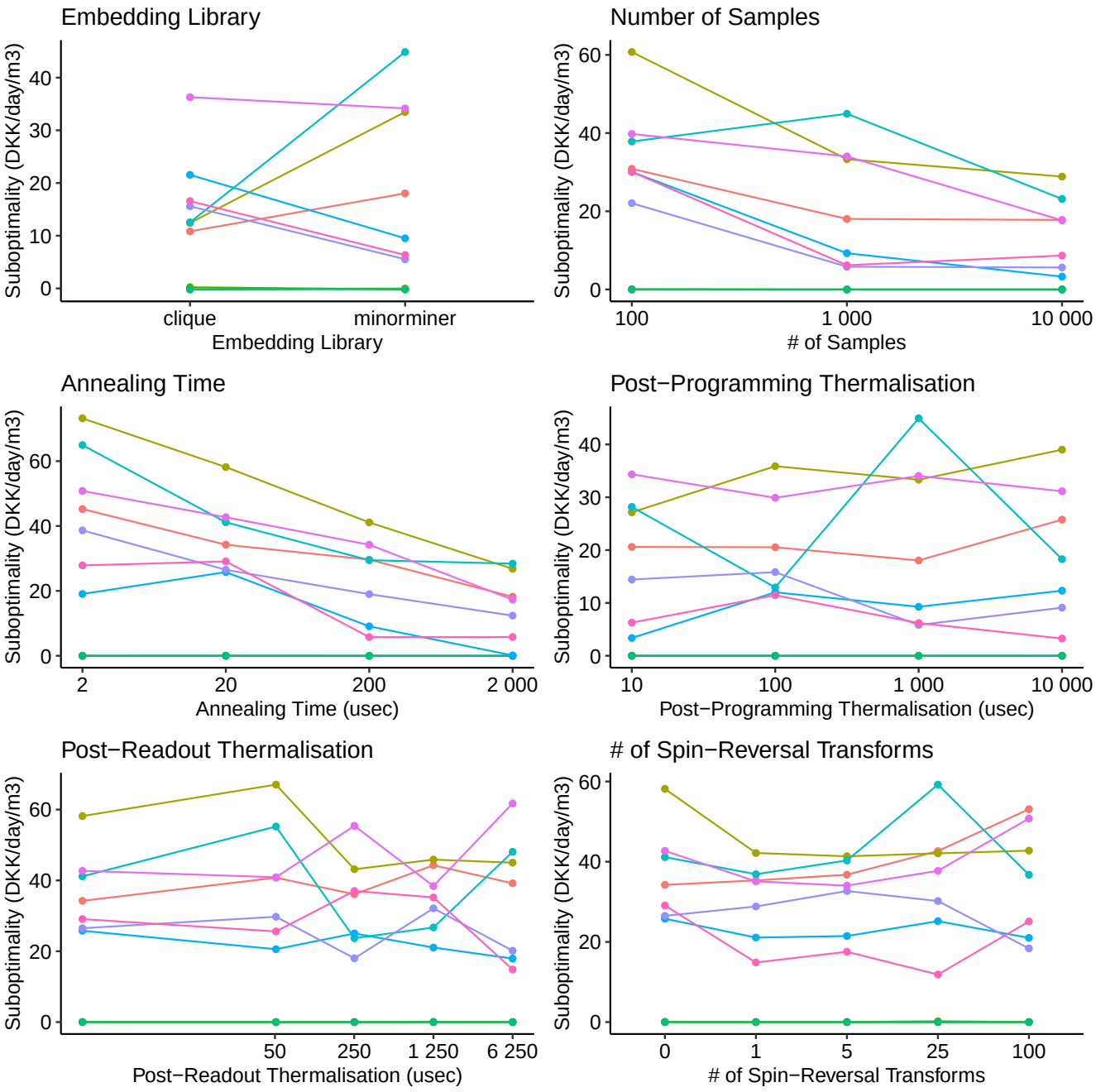

Figure 6. Effect of various control parameters of D-Wave's *Advantage* QPU on its performance for the QNLP adaptation of the biomass-selection problem described in Section 2.1. Same ten problems were used in all figures. Number of biomasses (K) is 21, and number of digits (M) is 3, i.e., 63 logical bits.

QNLP can also be used as a local-optimisation module in global algorithms such as TR. A key difference between standard methods for solving the TR 'subproblem' and QNLP is that the latter incorporates the bound constraints - specifically parameters **a** and **c** in Eq. 3 - into the definition of the neighborhood, thus allowing global wrappers to overcome the well-known inefficiency of classical TR algorithms in dealing with bound constraints[26]. Also, the QNLP neighborhood is rectangular while standard TRs are spherical, and hence some convergence proofs from TR theory must be adapted for QNLP-based global algorithms. On a more practical level, and depending on the number of iterations and number of samples per iteration needed, the cost of running QA tasks on D-Wave may need to be reduced further before a widespread adoption of global optimisers built on top of QNLP.

While the performance observed for the *DW-2000Q* QPU was near-perfect all the way through the maximum feasible problem size, the observed lower performance for the newer *Advantage* QPU is interesting (despite our exploration of adjusting control parameters in Section 2.3.4). It is also counter-intuitive that the best performance for both devices are achieved in the high-chain-break regime.

There are many potential reasons for the observed performance of the *Advantage* QPU in our problem. (For an overview of the sources of error in D-Wave QPUs, see[27,28].) One hypothesis is that the fully-dense structure of our $\mathbf{Q}$ matrices lead to excessive ICE errors and/or thermal noise, or that the device calibration is based on sparse matrices and hence inconsistent with the errors induced by a dense matrix. It is known that the as minimum spectral gap (difference between the two smallest eigenvalues of the full Hamiltonian) becomes smaller, escaping the ground state during QA becomes more likely, thus necessitating a slower annealing process[29,30]. We observed an improvement in performance as annealing time was increased (Figure 6), but the performance gap between the two device generations remains to be explained. Further research into these observations may provide important insight into performance and optimal design of QPUs and potential differences between different optimisation problems, e.g., discrete/binary vs. continuous cost functions, or sparse vs. dense/full connectivity.

Our experiments on D-Wave focused on an NLP with bound constraints. While our framework can theoretically handle generic constraints, several practical points must be noted. First, inequality constraints contribute slack variables and hence increase the problem dimension (number of logical bits). Current qubit count and connectivity of D-Wave devices will be a limiting factor in conducting experiments with constraints included. Secondly, for each constraint there will be a corresponding penalty term and hence a penalty strength parameter (η), which must be selected/tuned along with the number of bits used to represent the slack variable. These tuning parameters determine whether the final answer will satisfy the constraint or - hopefully only mildly - violate the constraint, and how close we are able to get to the constraint boundary without violating it. Developing heuristic algorithms for resolving ineffective or redundant constraints, in order to avoid unnecessary dimension expansion is another area of investigation.

Our current version of QNLP assumes all parameters are continuous. Yet the QUBO-based QA framework of D-Wave is more naturally suited for integer programming. Therefore, extending QNLP to mixed-integer programming (combining continuous and discrete dimensions) appears to be a natural next step. Interestingly, hybrid-computing frameworks have been proposed to handle mixed-programming problems, where continuous optimisation sub-problems are assigned to classical computers while discrete sub-problems are tackled by QC[31]. A major challenge with hybrid approaches is that the overhead of data exchange and context switch between the two sides can erase much of the gain from leveraging QC. QNLP could offer an alternative, more efficient approach to addressing these optimisation problems.

We believe that the QNLP framework presented in this paper takes a significant step towards utilising alternative computing platforms and hardware such as QA and CIM for solving important optimisation problems, including those related to green energy production. We envisage a rapid expansion and application of this framework, supported by improvements in various hardware technologies and their broader accessibility.

4 Materials and Methods

4.1 Nature Energy Data

Biochemical methane potential (BMP) tests were used to determine the methane potential and biodegradability of the different biomass substrates in batch mode using the Automatic Methane Potential Test System II (AMPTS® II) from Bioprocess Control. The biomass substrates were obtained from various local distributors in Denmark. In the test, a substrate was mixed with a filtrated anaerobic bacteria culture (substrate-to-inoculum ratio 1:4 to 1:2) freshly retrieved from an active primary digester from a local biogas plant in Denmark (NE Midtfyn A/S). Total solids (TS) and volatile solids (VS) were measured on all substrates according to standard procedures. 500 ml bottles containing inoculum and the substrate were kept under thermophilic conditions at a temperature of 52 °C and mixed in a 60 sec on/60 sec off sequence for a period of 30 days. Methane and carbon dioxide are produced during the testing period due to the anaerobic degradation of the organic contents of the substrate. The methane generated from the substrate is then measured and methane production of the substrate is normalised by the mass of volatile solids added (Nml CH 4 /g VS), and after subtracting the methane production from a container of Microcrystalline cellulose, used as control.

The average cumulative methane production for each biomass is estimated by fitting experimental data with the cone model (Section 4.2) to find the kinetics constants, G_0 (maximum biogas potential of the substrate, Nml CH 4 /g VS), k (biogas production rate constant, day^{-1}) and n (shape factor). The fit is obtained by minimizing the sum of squared differences between the experimental and calculated values.

The cost per fresh weight used in optimisation experiments is the sum of two components: procurement cost and transportation cost. Both components were calculated as average across sourcing and delivery sites, using numbers provided by NE's finance department for the harvest year 2020-2021. Unit revenue of biomethane is based on the 2020 figure provided by NE, and is the sum of market price of methane (1.5 DKK/Nm3) and subsidies (4.5 DKK/Nm3).

Note that, to protect sensitive business information, numbers presented in Table 1 are slightly modified from actual numbers used in optimisation experiments.

4.2 Biomass Selection Problem

4.2.1 Cone Model

In the cost function of Eq. 2, we need to specify the yield functions $\mathbf{Y}(X) = \begin{bmatrix} Y_1(X) & \dots & Y_K(X) \end{bmatrix}^\top$. The functions $Y_k()$ and their first and second derivatives can be described as

$$Y(X) = G_0\, y(\frac{V}{X};\theta) \tag{11a}$$

$$Y'(X) = G_0\,(-\frac{V}{X^2})\, y'(\frac{V}{X};\theta) \tag{11b}$$

$$Y''(X) = G_0\,(\frac{V}{X^2})\left((\frac{2}{X})\, y'(\frac{V}{X};\theta) + (\frac{V}{X^2})\, y''(\frac{V}{X};\theta)\right) \tag{11c}$$

where V is the active volume of the reactor, thus making V/X the Hydraulic Retention Time (HRT) of the reactor. G_0 is the maximum methane produced from a unit (volume) of the biomass, θ is the vector of (known) parameters of the production model, and $y()$ is the normalised yield curve, approaching 1 as HRT goes to infinity. We have dropped the subscript k from y, Y, and θ in the above to avoid clutter. In this paper, we use the Cone model of yield[18]:

$$y(t;k,n) = \left[1 + (kt)^{-n}\right]^{-1} \tag{12a}$$

$$y'(t;k,n) = (nk)\,(kt)^{-(n+1)}\,\left[1 + (kt)^{-n}\right]^{-2} \tag{12b}$$

$$y''(t;k,n) = (nk^2)\,(kt)^{-(n+2)}\,\left[1 + (kt)^{-n}\right]^{-2}\left\{(2n)\,(kt)^{-n}\,\left[1 + (kt)^{-n}\right]^{-1} - (n+1)\right\} \tag{12c}$$

Note that, in the above, k is one of the parameters of the cone mode, and not the biomass index. To calculate the gradient and Hessian of $f()$, we note that

$$\partial x_{k'}/\partial x_k = \delta_{k,k'}, \tag{13a}$$

$$\partial X/\partial x_k = 1 \tag{13b}$$

Applying the chain rule, we get:

$$\frac{\partial f}{\partial x_k} = -c_k + r\left(Y_k(X) + \sum_{l=1}^{K} Y'_l(X)\, x_l\right) \tag{14}$$

with $Y'_k(X) \equiv dY_k/dX$. In vector form:

$$\mathbf{g}_0 = -\mathbf{c} + r\left(\mathbf{Y} + (\mathbf{Y}'^\top \mathbf{x})\,\mathbf{1}\right) \tag{15}$$

More algebra leads to the following second derivative expression:

$$\frac{\partial^2 f}{\partial x_k\, \partial x_{k'}} = r\left\{Y'_k(X) + Y'_{k'}(X) + \sum_{l=1}^{K} Y''_l(X)\, x_l\right\} \tag{16}$$

In vector form:

$$\mathbf{H}_0 = r\left\{\mathbf{Y}'\,\mathbf{1}^\top + \mathbf{1}\,\mathbf{Y}'^\top + (\mathbf{Y}''^\top \mathbf{x})\,\mathbf{J}\right\}, \tag{17}$$

where $\mathbf{J}$ is a $K \times K$ matrix of ones: $\mathbf{J} \equiv \mathbf{1}\mathbf{1}^\top$. As expected, the Hessian is symmetric, i.e., $\frac{\partial^2 f}{\partial x_k\, \partial x_{k'}} = \frac{\partial^2 f}{\partial x_{k'}\, \partial x_k}$. It is easy to verify that $\mathbf{H}_0$ is fully-dense since each of the three constituent terms in Eq.17 are fully-dense, and there is no reason for their corresponding elements to cancel out in general.

4.2.2 Initialisation

QNLP starts with a quadratic approximation of the cost function in the neighborhood of an initial point (see Eq. 4). Here we describe the approach used for generating the initial points for experiments reported in this paper.

Figure 1 (panel **D**): Number of biomass types was given values of 3, 9, 15, 21 (increments of 6). For each value, 1000 runs was conducted. In each run, a random subset - including a random order - of biomass types from Table 1 were selected. The first value for $\mathbf{x}_0$ was chosen to be the univariate optimal value, i.e., the value that would maximise the reactor profit (unit volume) assuming that only that single biomass type was fed into the reactor. For all other biomass types, their corresponding entry in $\mathbf{x}_0$ was set to zero.

Figure 3 (panel **D**): Five biomass types were used, and two values for M (number of digits used to represent each dimension) were selected for estimating the discretisation error: 2 and 5. Reactor volume was assumed to be 1.0 (normalised). In each of the 1000 runs, $\mathbf{x}_0$ was chosen as follows. Each element was selected from a uniform distribution between $1e^{-3}$ and $2/15$. This ensured that the average HRT across all runs is close to 3 days.

Figure 5: Number of biomass types was given values of 10, 15, 21, 25. (The last value was only used with the *Advantage* QPU, due to the physical limitations of the *DW-2000Q* QPU.) For each combination of QPU, biomass type count and QA tuning parameters (chain strength multiplier and number of samples), we conducted 10 runs. In each run, we used the biomass with maximum univariate profitability as our 'anchor' biomass ('Deep Bedding - Chicken'). Next, we randomly selected the remaining biomass types, designating the first of those as 'contaminating' biomass and the rest as 'nuisance' biomass. All nuisance biomass types were given a value of zero for their $\mathbf{x}_0$ entry. For anchor biomass, its daily rate was selected from a uniform distribution centered on its univariate optimal value, with a range of ± 0.15. For contaminating biomass, its daily rate was selected from a uniform distribution with a minimum of 0.0 and a maximum of 0.15. With this setup, as we increase problem size (number of biomass types), the true minimum of the cost function within our rectangular neighborhood is always located at the univariate optimal point of the anchor biomass. Initial point is suboptimal due to 1- random deviations of anchor biomass from optimal value, 2- non-zero value for contaminating biomass. As we increase problem size (number of nuisance biomass types), QA will be tested to 'ignore' the nuisance dimensions and find the true minimum.

Figure 6: Same 10 problems corresponding to the previous figure and 21 biomasses were used.

4.3 QNLP

Below, we 1- elaborate the *vec* trick used in arriving at Eq. 10, 2- prove Result 3 regarding discretisation error of QNLP, and 3- extend Eq. 10 to include linear and nonlinear constraints, equality and inequality.

4.3.1 Unconstrained Case

Combining Equations 5 and 7, we get:

$$\mathbf{x} = \mathbf{a} + \Delta \mathbf{Z} \mathbf{b} \tag{18}$$

Using the 'vec' trick, $\text{vec}(ABC) = (C^\top \otimes A)\,\text{vec}(B)$, we can express $\mathbf{x}$ as a linear function of $\mathbf{z} = \text{vec}(\mathbf{Z})$, where $\text{vec}(\mathbf{Z})$ of the K-by-M matrix $\mathbf{Z}$ is a vector of length $K \times M$ resulting from stacking the M columns of $\mathbf{Z}$. Taking note that $\Delta \mathbf{Z} \mathbf{b}$ is a vector of length K, and thus $\Delta \mathbf{Z} \mathbf{b} = \text{vec}(\Delta \mathbf{Z} \mathbf{b})$, we have:

$$\Delta \mathbf{Z} \mathbf{b} = (\mathbf{b}^\top \otimes \Delta)\,\mathbf{z} \tag{19}$$

which is reflected in Equation 8a.

Deriving Eq. 10 from Eq. 4 is mostly routine algebra, while noting that for a binary variable z, we have $z^2 = z$. Therefore, for a binary vector $\mathbf{z}$:

$$\mathbf{u}^\top \mathbf{z} = \mathbf{z}^\top \text{diag}(\mathbf{u})\,\mathbf{z} \tag{20}$$

4.3.2 Proof of Denseness

Proof. Since the second term on the right-hand side of Eq. 10 is diagonal, we focus on the first term to prove denseness:

$$\mathbf{A}^\top \mathbf{H}_0 \mathbf{A} = \left(\mathbf{b}^\top \otimes \Delta\right)^\top \mathbf{H}_0 \left(\mathbf{b}^\top \otimes \Delta\right) \tag{21}$$

Note that

$$\mathbf{b}^\top \otimes \Delta = \begin{bmatrix} b_1\Delta & b_2\Delta & \dots & b_M\Delta \end{bmatrix} \tag{22}$$

and therefore

$$\mathbf{H}_0 \left(\mathbf{b}^\top \otimes \Delta\right) = \begin{bmatrix} b_1\mathbf{H}_0\Delta & b_2\mathbf{H}_0\Delta & \dots & b_M\mathbf{H}_0\Delta \end{bmatrix} \tag{23}$$

Next, we take advantage of the distributive property of transposition over Kronecker product:

$$\left(\mathbf{b}^\top \otimes \Delta\right)^\top = \mathbf{b} \otimes \Delta^\top = \begin{bmatrix} b_1\Delta \\ b_2\Delta \\ \vdots \\ b_M\Delta \end{bmatrix} \tag{24}$$

Combining the above two, we obtain

$$\mathbf{A}^\top \mathbf{H}_0 \mathbf{A} = \begin{bmatrix} b_1\Delta \\ b_2\Delta \\ \vdots \\ b_M\Delta \end{bmatrix} \begin{bmatrix} b_1\mathbf{H}_0\Delta & b_2\mathbf{H}_0\Delta & \dots & b_M\mathbf{H}_0\Delta \end{bmatrix} = \begin{bmatrix} b_1^2\,\Delta\mathbf{H}_0\Delta & b_1b_2\,\Delta\mathbf{H}_0\Delta & \dots & b_1b_M\,\Delta\mathbf{H}_0\Delta \\ b_1b_2\,\Delta\mathbf{H}_0\Delta & b_2^2\,\Delta\mathbf{H}_0\Delta & \dots & b_2b_M\,\Delta\mathbf{H}_0\Delta \\ \dots & \dots & \ddots & \dots \\ b_1b_M\,\Delta\mathbf{H}_0\Delta & b_2b_M\,\Delta\mathbf{H}_0\Delta & \dots & b_M^2\,\Delta\mathbf{H}_0\Delta \end{bmatrix} \tag{25}$$

Finally, note that

$$(\Delta\mathbf{H}_0\Delta)_{i,j} = \sum_k \sum_{k'} \Delta_{i,k}\,\mathbf{H}_{0,k,k'}\,\Delta_{k',j} = \delta_i\,\delta_j\,\mathbf{H}_{0,i,j} \tag{26}$$

where we have taken advantage of Δ being diagonal. Since $\delta_i > 0, \forall i$ and also $b_k > 0, \forall k$, we conclude that $\mathbf{A}^\top \mathbf{H}_0 \mathbf{A}$ is fully-dense as long as $\mathbf{H}_0$ is fully dense. □

We also note that, Eq. 25 can be easily re-written as

$$\mathbf{A}^\top \mathbf{H}_0 \mathbf{A} = (\mathbf{b}\,\mathbf{b}^\top) \otimes (\Delta\mathbf{H}_0\Delta) \tag{27}$$

4.3.3 Discretisation Error

We calculate an upper bound on the error caused by replacing the continuous $\mathbf{x}$ in Eq. 4 with a discrete one per Eq. 5. The error would be due to the true minimum happening in-between grid points, and at a value lower than the observed minimum.

The worst-case scenario - i.e., maximum error between observed and true minimum - is when we have two neighboring points on the grid both being the observed minimums, and the true minimum lying halfway between them. Since we are minimising a quadratic function, its intersection with any plane is also of quadratic form. In particular, consider that $\mathbf{x}$ is allowed to move along the direction indicated by the unit vector $\hat{\beta}$, around the origin located at α:

$$\mathbf{x}(u) = \alpha + u\,\hat{\beta} \tag{28}$$

Plugging the above back into Eq. 4, we obtain a quadratic form with the second derivative given by

$$f''(u) = \sum_k \lambda_k\,\gamma_k^2 \tag{29}$$

where λ_k's are the eigenvalues of $\mathbf{H}$ and γ_k's are the coefficients of $\hat{\beta}$ in the eigenbasis of $\mathbf{H}$, i.e., $\hat{\beta} = \sum_k \gamma_k\,\hat{\mathbf{v}}_k$ with $\hat{\mathbf{v}}_k$ being the k'th eigenvector of $\mathbf{H}$. To see the above, we simply note that

$$\mathbf{x}^\top \mathbf{H}\,\mathbf{x} = (\alpha^\top + u\,\hat{\beta}^\top)\,\mathbf{H}\,(\alpha + u\,\hat{\beta}) = \left(\hat{\beta}^\top \mathbf{H}\,\hat{\beta}\right) u^2 + \dots \tag{30}$$

Using the eigendecomposition property, $\mathbf{H}\,\hat{\mathbf{v}}_k = \lambda_k\,\hat{\mathbf{v}}_k$ readily leads to Eq. 29.

Noting that, for the unit vector $\hat{\beta}$ to have a norm of 1, we must have $\sum_k \gamma_k^2 = 1$, it is easy to conclude that maximum second deriative occurs when $\hat{\beta}$ points along the direction of largest positive eigenvalue of $\mathbf{H}$, which we simply call λ for brevity.

On the other hand, for a twice-differentiable cost function, minimums happen where the gradient vector is zero. For the function to have an interior minimum, it cannot be lower by more than $\frac{1}{2}\,\lambda d^2$, where d is the minimum distance of the point from any of the vertices of the grid, which has a resolution vector ε. This minimum distance has a maximum of $\frac{1}{2}\,(\varepsilon^\top\,\varepsilon)^{\frac{1}{2}}$. (See lemma below.) Combining the above two proves our result.

Lemma 1. *Consider a point inside a K-dimensional hypercube of unit length. Let's call the minimum distance of the point from all K vertices of the hypercube d. Maximum of d is* $\frac{\sqrt{K}}{2}$*, which occurs when the point is at the center of the hypercube's main diagonal.*

Proof. Without loss of generality, assume that the hypercube vertices having coordinates consisting of 0's and 1's only, i.e., it lies in the first orthant, its sides are aligned with coordinates, and has one vertex at the origin. The minimum distance of an interior point from the vertices - i.e., the inner optimisation problem - can be cast as a QUBO with the cost function $(\mathbf{x}-\mathbf{y})^\top(\mathbf{x}-\mathbf{y})$, where $\mathbf{x}$ is the binary vector representing hypercube vertices, and $\mathbf{y}$ is the location of the interior point. The resulting diagonal $\mathbf{Q}$ matrix associated with this QUBO is $\mathrm{I}_K - 2\,\mathrm{diag}(\mathbf{y})$, and the cost function has a minimum of $\sum_k \min(1-2y_k, 0)$. Therefore, the outer optimisation (maximisation) problem has the objective function $\sum_k \left\{y_k^2 + \min(1-2y_k, 0)\right\}$, subject to constraints $0 \le y_k \le 1$, $\forall k = 1, \ldots, K$. This can be easily verified to have a maximum of $\frac{\sqrt{K}}{2}$, located at $\mathbf{y} = \frac{1}{2}\,\mathbf{1_K}$. Generalisation to an orthotope or hyperrectangle can be done via a simple rescaling of coordinates. □

As seen in Figure 3 (panel **D**), the upper bound is rather conservative in our experiments, where observed improvement from increasing grid resolution ($M = 2$ to $M = 5$) never exceeded more than $1/5$ of the upper bound. (Of course, it is also possible that increasing M beyond 5 would have significantly increased the observed improvement, but that is unlikely since often such successive improvements follow a geometric series.) It may be possible to calculate tighter upper bounds, but that must be weighed against any potential computational burden of such calculations, e.g., in each iteration of a global optimisation algorithm using QNLP.

4.3.4 Linear Inequality Constraint

The inequality constraint

$$\mathbf{u}^\top \mathbf{x} \le v \tag{31}$$

can be transformed - using Eq. 8a - into the following binary form

$$\mathbf{u'}^\top \mathbf{z} \le v' \tag{32}$$

with the following definitions:

$$\begin{cases} \mathbf{u'} &= \mathbf{A}^\top \mathbf{u} & \text{(33a)} \\ v' &= v - \mathbf{u}^\top (\mathbf{x}_0 + \mathbf{d}) & \text{(33b)} \end{cases}$$

where $\mathbf{A}$ and $\mathbf{d}$ are defined by Eqs. 8c and 8b. Next, following[32], we introduce a *slack variable*, s:

$$\mathbf{u'}^\top \mathbf{z} \le v' \;\rightarrow\; \mathbf{u'}^\top \mathbf{z} + s = v' \quad s \ge 0. \tag{34}$$

We can tighten the limits on s by taking advantage of $\mathbf{z}$ being a binary vector of length KM

$$\sum_{n=1}^{KM} u'_n \mathrm{I}[u'_n < 0] \le \mathbf{u'}^\top \mathbf{z} \le \sum_{n=1}^{KM} u'_n \mathrm{I}[u'_n \ge 0] \tag{35}$$

We use Eq. 34 to replace $\mathbf{u'}^\top \mathbf{z}$ with $v' - s$ in the above. After some re-arranging, and noting that $s \ge 0$, we obtain:

$$\begin{cases} s_{min} &\le s \le s_{max} & \text{(36a)} \\ s_{min} &\equiv \max\{v' - \sum_{n=1}^{KM} u'_n \mathrm{I}[u'_n \ge 0], 0\} & \text{(36b)} \\ s_{max} &\equiv v' - \sum_{n=1}^{KM} u'_n \mathrm{I}[u'_n < 0] & \text{(36c)} \end{cases}$$

We can now use $\mathbf{z}_s$, a binary vector of length D, to represent s, as below:

$$s = s_{min} + \mathbf{b}_s^\top \mathbf{z}_s \tag{37a}$$

$$\mathbf{b}_s \equiv \frac{s_{max} - s_{min}}{2^D - 1} \begin{bmatrix} 1 & 2 & \cdots & 2^{D-1} \end{bmatrix} \tag{37b}$$

To enforce the inequality constraint of Eq. 31, we add the following quadratic penalty term to our cost/energy function of Eq. 10:

$$E_c(\mathbf{z},\mathbf{z}_s) = \eta\,(\mathbf{u}'^{\top}\mathbf{z} + s_{min} + \mathbf{b}_s^{\top}\mathbf{z}_s - v')^2 \tag{38}$$

where η is a tuning parameter that determines the relative strength/importance of the penalty term vs. the original term. Combining the penalty term and original cost function of Eq 10, we arrive at the standard quadratic form with the following expanded coupling matrix

$$\mathbf{Q}^* = \begin{bmatrix} \mathbf{Q} + \mathbf{Q}^i_{11} & \mathbf{Q}^i_{12} \\ \mathbf{Q}^{i,\top}_{12} & \mathbf{Q}_{22} \end{bmatrix} \tag{39}$$

with the following definitions:

$$\begin{cases} \mathbf{Q}^i_{11} &= \eta\left\{\mathbf{u}'\mathbf{u}'^{\top} + 2\,(s_{min} - v')\,\mathrm{diag}(\mathbf{u}')\right\} & (40a)\\ \mathbf{Q}^i_{12} &= \eta\,\mathbf{u}'\,\mathbf{b}_s^{\top} & (40b)\\ \mathbf{Q}^i_{22} &= \eta\left\{\mathbf{b}_s\,\mathbf{b}_s^{\top} + 2\,(s_{min} - v')\,\mathrm{diag}(\mathbf{b}_s)\right\} & (40c) \end{cases}$$

applied to the binary vector $\mathbf{z}^*$ of length $KM + D$, defined as:

$$\mathbf{z}^* \equiv \begin{bmatrix} \mathbf{z} \\ \mathbf{z}_s \end{bmatrix} \tag{41}$$

Note that adding the inequality constraint has caused the size of the problem to expand by D, which is the number of binary digits used to represent the slack variable.

4.3.5 Linear Equality Constraints

Equality constraints do not need slack variables, and hence only contribute to QUBO as follows:

$$\mathbf{Q}^* = \mathbf{Q} + \mathbf{Q}^e \tag{42}$$

with

$$\mathbf{Q}^e = \eta\left\{\mathbf{u}'\,\mathbf{u}'^{\top} - 2v'\,\mathrm{diag}(\mathbf{u}')\right\} \tag{43}$$

4.3.6 Multiple Linear Constraints

To handle multiple constraints, the above process has to be repeated for each constraint. The number of binary digits used to represent the slack variable, as well as its corresponding η, can be the same or different across constraints.

Consider the following set of N_i inequality and N_e equality linear constraints:

$$\mathbf{U}_i\,\mathbf{x} \le \mathbf{v}_i \tag{44a}$$
$$\mathbf{U}_e\,\mathbf{x} = \mathbf{v}_e \tag{44b}$$

with $\mathbf{U}_{i/e} = \begin{bmatrix} \mathbf{u}_{i/e,1} & \cdots & \mathbf{u}_{i/e,N_{i/e}} \end{bmatrix}^{\top}$ being $K \times N_{i/e}$ matrix resulting from row-wise stacking coefficients of individual inequality/equality constraints. Similarly, $\mathbf{v}_{i/e} = \begin{bmatrix} v_{i/e,1} & \cdots & v_{i/e,N_{i/e}} \end{bmatrix}$. The operators $\le$ and $=$ are interpreted in an element-wise fashion.

Similar to before, the following transformations

$$\begin{cases} \mathbf{u}'_{i/e,n} &= \mathbf{A}^{\top}\,\mathbf{u}_{i/e,n} & (45a)\\ v'_{i/e,n} &= v_{i/e,n} - \mathbf{u}^{\top}_{i/e,n}\,(\mathbf{x}_0 + \mathbf{d}) & (45b) \end{cases}$$

allow us to transform the above constraints from $\mathbf{x}$ space to $\mathbf{z}$ space

$$\mathbf{U}'_i\,\mathbf{z} \le \mathbf{v}'_i \tag{46a}$$
$$\mathbf{U}'_e\,\mathbf{z} = \mathbf{v}'_e \tag{46b}$$

We introduce the following N_i slack variables for inequality constraints, along with their lower and upper bounds:

$$\begin{cases} s_{n,min} & \leq s_n \leq s_{n,max} & \text{(47a)} \\ s_{n,min} & \equiv \max\{v'_n - \sum_{m=1}^{KM} u'_{i,n,m}\, \mathrm{I}[u'_{i,n,m} \geq 0], 0\} & \text{(47b)} \\ s_{n,max} & \equiv v'_n - \sum_{m=1}^{KM} u'_{i,n,m}\, \mathrm{I}[u'_{i,n,m} < 0] & \text{(47c)} \end{cases}$$

where $n = 1, \ldots, N_i$. Each slack variable is represented by D_n bits:

$$s_n = s_{n,min} + \mathbf{b}_{s,n}^\top \mathbf{z}_{s,n} \tag{48a}$$

$$\mathbf{b}_{s,n} \equiv \frac{s_{n,max} - s_{n,min}}{2^{D_n} - 1} \begin{bmatrix} 1 & 2 & \cdots & 2^{D_n - 1} \end{bmatrix} \tag{48b}$$

Each inequality and equality constraint contributes a penalty term to the QUBO:

$$E_{i,n}(\mathbf{z}, \mathbf{z}_{s,n}) = \eta_{i,n} \left(\mathbf{u}'^{\top}_{i,n} \mathbf{z} + s_{n,min} + \mathbf{b}_{s,n}^\top \mathbf{z}_{s,n} - v'_{i,n}\right)^2, \quad n = 1, \ldots, N_i \tag{49a}$$

$$E_{e,n}(\mathbf{z}) = \eta_{e,n} \left(\mathbf{u}'^{\top}_{e,n} \mathbf{z} - v'_{e,n}\right)^2, \quad n = 1, \ldots, N_e \tag{49b}$$

Combining all constraints, we obtain a QUBO with the coupling matrix $\mathbf{Q}^*$ which is best defined in terms of its constituent $(N_i + 1)^2$ blocks, $\mathbf{Q}^*_{p,q}$ of dimensions $T(p) \times T(q)$. The dimension function $T(.)$ is given by:

$$T(p) = \begin{cases} KM, & p = 1 \\ D_{p-1}, & p = 2, \ldots, N_i + 1 \end{cases} \tag{50}$$

The blocks are defined below:

$$\mathbf{Q}^*_{p,q} = \begin{cases} \mathbf{Q} + \sum_{n=1}^{N_i} \eta_{i,n} \left\{ \mathbf{u}'_{i,n} \mathbf{u}'^{\top}_{i,n} + 2\left(s_{n,min} - v'_n\right) \mathrm{diag}(\mathbf{u}'_{i,n}) \right\} + \sum_{n=1}^{N_e} \eta_{e,n} \left\{ \mathbf{u}'_{e,n} \mathbf{u}'^{\top}_{e,n} - 2 v'_n \mathrm{diag}(\mathbf{u}'_{e,n}) \right\}, & p = 1, q = 1 \\ \eta_{i,p-1} \left\{ \mathbf{b}_{s,p-1} \mathbf{b}_{s,p-1}^\top + 2\left(s_{p-1,min} - v'_{p-1}\right) \mathrm{diag}(\mathbf{b}_{s,p-1}) \right\}, & p = 2, \ldots, N_i + 1, q = p \\ \eta_{i,q-1}\, \mathbf{u}'_{i,q-1}\, \mathbf{b}_{s,q-1}^\top, & p = 1, q = 2, \ldots, N_i + 1 \\ \mathbf{Q}^{*\top}_{q,p}, & p = 2, \ldots, N_i + 1, q = 1 \\ 0, & \text{otherwise} \end{cases} \tag{51}$$

As indicated above, only the first row, first column and the diagonal blocks of $\mathbf{Q}^*$ are non-zero. This is made more clear in the following:

$$\mathbf{Q}^* = \begin{bmatrix} \mathbf{Q}^*_{1,1} & \mathbf{Q}^*_{1,2} & \cdots & \mathbf{Q}^*_{1,N_i+1} \\ \mathbf{Q}^*_{2,1} & \mathbf{Q}^*_{2,2} & \mathbf{0} & \mathbf{0} \\ \vdots & \mathbf{0} & \ddots & \mathbf{0} \\ \mathbf{Q}^*_{N_i+1,1} & \mathbf{0} & \mathbf{0} & \mathbf{Q}^*_{N_i+1,N_i+1} \end{bmatrix} \tag{52}$$

It can be seen from the above that $\mathbf{Q}^*$ is not fully dense, as the slack variables corresponding to different inequality constraints do not have interaction terms. This allows constrained problems to be embedded on D-Wave QPUs more easily.

4.3.7 General Case - Nonlinear Constraints

Consider the following nonlinear, inequality constraint

$$w(\mathbf{x}) \leq 0 \tag{53}$$

where $w()$ is a generic, possibly nonlinear, function. First-order Taylor-series around $\mathbf{x} = \mathbf{x}_0$ gives

$$w(\mathbf{x}_0) + \left(\nabla w|_{\mathbf{x}_0}\right)^\top (\mathbf{x} - \mathbf{x}_0) \leq 0 \tag{54}$$

Simple re-arrangement of terms gives us

$$\mathbf{u}^\top \mathbf{x} \leq v \tag{55}$$

with the following definitions:

$$\begin{cases} \mathbf{u} \equiv & \nabla w|_{\mathbf{x}_0} & \text{(56a)} \\ v \equiv & \left(\nabla w|_{\mathbf{x}_0}\right)^\top \mathbf{x}_0 - w(\mathbf{x}_0) & \text{(56b)} \end{cases}$$

We can use the above in the formulas developed before. The case for equality constraints is identical.

4.4 Quantum Annealing on D-Wave

4.4.1 Overview of Quantum Annealing

QA is based on the adiabatic theorem which, in simplified terms, states that a quantum mechanical system starting in an eigenstate - e.g., ground state - of a slowly-changing Hamiltonian will remain in its corresponding eigenstate during system evolution. A transverse-field Ising-model implementation starts out the system - consisting of a collection of interacting quantum bits or qubits - in the initial/tunneling Hamiltonian with a trivial ground state, and slowly introduces the final/problem Hamiltonian, corresponding to the QUBO being minimised. By the end of annealing, only the problem Hamiltonian remains, at which point the qubit spins are 'measured' and the classical bits corresponding to the minimum energy - or a value close to it - are returned:

$$\mathscr{H}_{ising}(s) = -\frac{A(s)}{2}\left(\sum_i \hat{\sigma}_x^{(i)}\right) + \frac{B(s)}{2}\left(\sum_i h_i\,\hat{\sigma}_z^{(i)} + \sum_{i>j} J_{i,j}\,\hat{\sigma}_z^{(i)}\,\hat{\sigma}_z^{(j)}\right) \tag{57}$$

In the above, s is the normalised annealing time varying between 0 and 1. $A(s)$ and $B(s)$ control the relative strength of initial and final Hamiltonians, such as $A(0) >> B(0)$ and $A(1) << B(1)$. Quantum annealing is similar to (classical) simulated annealing (SA), with the key difference being that state transitions in QA are due to quantum tunneling rather than thermal fluctuations in SA.

4.4.2 Control Parameters

Number of reads or samples determines how many anneal-readout cycles QPU should perform. Collecting more than one sample is important since various sources of error may cause a single anneal cycle to deviate from the ground state of the intended problem Hamiltonian. The best result among all samples is often chosen as the final output from QA solver. Time-series of sample energies can be examined for evidence of noise accumulation, e.g., due to insufficient heat dissipation after each readout.

Embedding library refers to the algorithm for mapping the problem graph - corresponding to **Q** - to the QPU connectivity graph, such that the problem graph becomes a minor of the QPU graph. The goal is to create indirect connections between vertices that cannot be directly connected due to sparseness of the QPU graph. Two libraries are provided by D-Wave: a heuristic, general-purpose library called minorminer embedding[33], and a specialised one for embedding fully-connected graphs, called clique embedding[34]. Note that embedding itself can be time consuming, especially for large graphs, but for fully-dense matrices it can be pre-calculated once for each graph size.

Chain strength controls the relative importance of chain-coherence penalty term vs. the original QUBO cost function. Low values lead to frequent chain breaks and hence inconsistent qubit values representing a single logical bit, while high values lead to mis-utilisation of limited dynamic range of QPU coupling strengths and insensitivity of final solutions to the desired cost function. D-Wave offers two heuristics for setting chain strength: 1) *scaled*, which sets chain strength equal to maximum absolute value of **Q** entries, and 2) a so-called *uniform torque compensation* method.

Chain break resolution determines the logic for resolving inconsistent bits within a chain. Options offered by D-wave are: 1) discard any samples with any broken chain, 2) fix each broken chain by taking majority vote among chain bits, 3) use weighed random choice, 4) minimize local energy. For dense, high-dimensional problems involving many chains, most samples are bound to have at least one chain break and hence the discard strategy is not practical in those cases.

Annealing time determines the speed with which the Hamiltonian evolves from the tunneling term to the problem term (see Section 4.4.1). Previous research[35,36] indicates that smaller annealing times are needed to maintain performance for problems with small minimum spectral gap. However, increased annealing time has an obvious computational cost.

Programming thermalisation defines the length of delay (in microseconds) after 'programming' the QPU with the **Q** matrix values, and before starting the annealing cycles. This delay allows for dissipation from generated in the programming process. This is done only once at the beginning of the anneal-readout cycles. For both *DW-2000Q* and *Advantage* devices, the acceptable range of this parameter is 0-10,000 microseconds, with a default value of 1,000 microseconds.

Readout thermalisation defines the length of time (in microseconds) at the end of each anneal-readout cycle to pause before starting the next anneal. This allows for heat removal caused by reading out the qubit values. For both *DW-2000Q* and *Advantage* devices, the acceptable range for this parameter is 0-10,000 microseconds, with a default value of zero.

Post-processing refers to strategies for improving quality of solutions returned by QPU, e.g., by doing a local search in the neighborhood of each sample returned by the QPU, using classical solvers.

Spin reversal transforms helps reduce the effect of programming biases and errors, but requires programming the QPU for each sample, hence adding to total sampling time and amount of heat generated in the device.

References

1. World biogas association. https://tinyurl.com/2vufvm5n. Accessed: 2021-04-13.
2. Global potential of biogas. https://tinyurl.com/2tk6nw4d. Accessed: 2021-04-13.
3. Yoshimura, C. *et al.* Uncertain behaviours of integrated circuits improve computational performance. *Sci. reports* **5**, 1–12 (2015).
4. Tsukamoto, S., Takatsu, M., Matsubara, S. & Tamura, H. An accelerator architecture for combinatorial optimization problems. *Fujitsu Sci. Tech. J* **53**, 8–13 (2017).
5. Sutton, B., Camsari, K. Y., Behin-Aein, B. & Datta, S. Intrinsic optimization using stochastic nanomagnets. *Sci. reports* **7**, 1–9 (2017).
6. Parihar, A., Shukla, N., Jerry, M., Datta, S. & Raychowdhury, A. Vertex coloring of graphs via phase dynamics of coupled oscillatory networks. *Sci. reports* **7**, 1–11 (2017).
7. Tait, A. N. *et al.* Neuromorphic photonic networks using silicon photonic weight banks. *Sci. reports* **7**, 1–10 (2017).
8. Zhang, W. *et al.* Neuro-inspired computing chips. *Nat. Electron.* **3**, 371–382 (2020).
9. Hamerly, R. *et al.* Experimental investigation of performance differences between coherent ising machines and a quantum annealer. *Sci. advances* **5**, eaau0823 (2019).
10. Boixo, S. *et al.* Evidence for quantum annealing with more than one hundred qubits. *Nat. physics* **10**, 218–224 (2014).
11. Harper, R. & Flammia, S. T. Fault-tolerant logical gates in the ibm quantum experience. *Phys. review letters* **122**, 080504 (2019).
12. Wright, K. *et al.* Benchmarking an 11-qubit quantum computer. *Nat. communications* **10**, 1–6 (2019).
13. Bromley, T. R. *et al.* Applications of near-term photonic quantum computers: software and algorithms. *Quantum Sci. Technol.* **5**, 034010 (2020).
14. Aramon, M. *et al.* Physics-inspired optimization for quadratic unconstrained problems using a digital annealer. *Front. Phys.* **7**, 48 (2019).
15. Marandi, A., Wang, Z., Takata, K., Byer, R. L. & Yamamoto, Y. Network of time-multiplexed optical parametric oscillators as a coherent ising machine. *Nat. Photonics* **8**, 937–942 (2014).
16. Sherrington, D. & Kirkpatrick, S. Solvable model of a spin-glass. *Phys. review letters* **35**, 1792 (1975).
17. Batstone, D. J. *et al.* The IWA anaerobic digestion model no 1 (ADM1). *Water Sci. technology* **45**, 65–73 (2002).
18. Zahan, Z., Othman, M. Z. & Muster, T. H. Anaerobic digestion/co-digestion kinetic potentials of different agro-industrial wastes: A comparative batch study for c/n optimisation. *Waste Manag.* **71**, 663–674 (2018).
19. Pardalos, P. M. & Vavasis, S. A. Quadratic programming with one negative eigenvalue is np-hard. *J. Glob. optimization* **1**, 15–22 (1991).
20. Nocedal, J. & Wright, S. J. Sequential quadratic programming. *Numer. optimization* 529–562 (2006).
21. Conn, A. R., Gould, N. I. & Toint, P. L. *Trust region methods* (SIAM, 2000).
22. Schulman, J., Levine, S., Abbeel, P., Jordan, M. & Moritz, P. Trust region policy optimization. In *International conference on machine learning*, 1889–1897 (PMLR, 2015).
23. Cobzaş, Ş., Miculescu, R. & Nicolae, A. *Lipschitz functions*, vol. 2241 (Springer, 2019).
24. D-wave QPU architecture: Topologies. https://docs.dwavesys.com/docs/latest/c_gs_4.html. Accessed: 2021-03-26.
25. D-wave leap. https://www.dwavesys.com/take-leap. Accessed: 2021-03-31.
26. Yuan, Y.-x. Recent advances in trust region algorithms. *Math. Program.* **151**, 249–281 (2015).
27. Ice: Dynamic ranges in h and j values. https://docs.dwavesys.com/docs/latest/c_qpu_1.html. Accessed: 2021-05-22.
28. Other factors affecting performance. https://docs.dwavesys.com/docs/latest/c_qpu_2.html. Accessed: 2021-05-22.
29. Morita, S. & Nishimori, H. Mathematical foundation of quantum annealing. *J. Math. Phys.* **49**, 125210 (2008).

30. Mishra, A., Albash, T. & Lidar, D. A. Finite temperature quantum annealing solving exponentially small gap problem with non-monotonic success probability. *Nat. communications* **9**, 1–8 (2018).

31. Ajagekar, A., Humble, T. & You, F. Quantum computing based hybrid solution strategies for large-scale discrete-continuous optimization problems. *Comput. & Chem. Eng.* **132**, 106630 (2020).

32. Glover, F., Kochenberger, G. & Du, Y. Quantum bridge analytics i: a tutorial on formulating and using qubo models. *4OR* **17**, 335–371 (2019).

33. Cai, J., Macready, W. G. & Roy, A. A practical heuristic for finding graph minors. *arXiv preprint arXiv:1406.2741* (2014).

34. Boothby, T., King, A. D. & Roy, A. Fast clique minor generation in chimera qubit connectivity graphs. *Quantum Inf. Process.* **15**, 495–508 (2016).

35. Jansen, S., Ruskai, M.-B. & Seiler, R. Bounds for the adiabatic approximation with applications to quantum computation. *J. Math. Phys.* **48**, 102111 (2007).

36. Lidar, D. A., Rezakhani, A. T. & Hamma, A. Adiabatic approximation with exponential accuracy for many-body systems and quantum computation. *J. Math. Phys.* **50**, 102106 (2009).

5 Author contributions statement

M.T.A.S developed the mathematical framework and contributed to software development. V.B.J. collected biogas data and parameters. M.J. contributed to problem definition, and supplied the biogas production assumptions and constraints. A.S.M. contributed to problem definition and software development. All authors reviewed the manuscript.